Numerical simulations of different bearings to obtain the surface tension through the finite element method

Behrouz Bohlouli[1], Sattar Jedari Salami[2*]

[1]Department of Mechanical Engineering, Damavand Branch, Islamic Azad University, Damavand, Iran

[2]Department of Mechanical Engineering, Central Tehran Branch, Islamic Azad University, Tehran, Iran

Abstract

Higher-performance tapered roller bearings are required to increase freight vehicle loads. More development is needed for the modeling tools and techniques utilized for subsurface contact stress evaluations, as the stress condition on railway bearing applications is rising. Railway-bearing contact geometries and heat treatment standards were first created under ideal load circumstances. Nonetheless, tapered roller bearings are subjected to various load conditions which are rarely ideal in railroad applications. Furthermore, there are frequent variations in bearing loads, railcar wear conditions, maintenance procedures, and reliability vs utilization expectations when comparing global rail markets. In the current research paper, the bearing with different special shapes is modeled using the finite element method under loading conditions. Also, the obtained results are compared to those obtained theoretically. The results reveal that the finite element modeling can predict the theoretical observations and finally, it can be concluded that the shapes of the bearings influence the stress distributions in the systems.

Keywords: Bearing; Finite element method; Theoretical concepts; Surface tension; Contact pressure

[*] Corresponding author; Sattar Jedari Salami; Associate Professor
Central Tehran branch, Islamic Azad University, Tehran, Iran
E-mail: sattar.salami@aut.ac.ir

1. Introduction

In the context of mechanics, a bearing is a crucial component that reduces friction between two moving parts [1]. It essentially allows for smooth and efficient rotation while minimizing energy loss due to rubbing or sliding. Bearings provide support and guidance to a rotating shaft, allowing it to turn with minimal resistance. This reduces wear and tear on the shaft and surrounding components, ultimately increasing the lifespan of the machinery [2]. There are various types of bearings, each suited for specific applications based on factors like load, speed, and operating environment. Some common types include ball bearings**,** roller bearings, plain bearings, and magnetic bearings. Bearings are ubiquitous across various industries and find use in automobiles, industrial machinery, aerospace, household applications, etc. Choosing the right type of bearing depends on various factors, including load capacity**,** speed, operating environment, accuracy and precision, cost, and maintenance requirements. By understanding the different types of bearings and their characteristics, engineers can select the optimal bearing solution for their specific application, ensuring efficient operation, extended equipment life, and optimal performance. Railway applications for bearings include wagons, locomotives, and rolling stock components to support wheels, axles, and rotary components[3].

When the bearing force exceeds the yield strength of the material, it can lead to deformation[4]. Too much load application on a small area can subject the material under the area to high stress, leading to failure[5]. A bearing failure occurs when the bearing fails to meet its expected life or performance levels, often causing a machine shaft to fail, and the machine it is a part of can break down. The consequences of bearing failure are far-reaching for your facility. These can include increased downtime, high maintenance costs, missed deliveries, loss of revenue, and, in some extreme cases, may injure workers. When a bearing fails, it negatively impacts your facility, your reputation, and your bottom line. That said, there are some preventative measures you can take to increase the lifespan of your bearings and prevent improper wear on them[6].

Due to the importance of the bearings in different industries, some articles about the bearings are briefly described here.

Cage friction measurements were initially reported by Molina and Gohar in 1977. A glass plate cage segment was attached around a revolving ball, and the angular deflection of a torsional spring was used to measure the torque applied to the cage segment. Records were kept for weights up to 40N and speeds up to 375 rpm. From the data, a friction coefficient was computed for comparison with a similar hydrodynamic lubrication model. Friction coefficient values in the experiments varied from 0.17 to 0.4 and were shown to decrease with an increase in applied stress. The results of their hydrodynamic lubrication model and the experiments agreed well [7]. In 1978, the researchers expanded on their analysis of hydrodynamic cage lubrication and provided design curves that illustrate the correlation between torque, cage pocket clearance, and ball placement within the pocket. It was demonstrated that the outcomes resembled those of a journal bearing a finite breadth. They concluded that a cage pocket's torque and power consumption depend more heavily on the pocket's size than on the ball's position within it. In 1985, Gentle and Pasdari reported friction measurements between a ball and a section of a cage. By comparing the torque production from a motor in dry and lubricated circumstances, they were able to determine the frictional torque on a submerged ball and cage for speeds ranging from 1000 to 25000 rpm[8]. Researchers looked at the impact of the ball's location in the cage pocket at speeds of up to 9000 rpm, but they were unable to measure the variation in friction that resulted from the ball's placement inside the cage. The ball's frictional torque had values between 1 Nmm at 1000 rpm and 6 Nmm at 6000 rpm[8]. Their experimental results closely matched an analytical model proposed by Gentle and Boness [9]. At low rotational speeds, Shaona and his colleague examined the friction between balls and a stamped ribbon cage. Friction coefficients under dry and lubricated circumstances were determined for various speeds between a rotating ball and cage [10]. A torque cell was fixed to half of a

stamped steel cage as part of the experimental setup. Up to 20 N of preload force was applied to the two bodies in contact, and the ball rotated at a maximum speed of 480 rpm. There were no observed patterns for the friction coefficient about speed or applied load; nevertheless, boundary lubrication was observed in the cage pocket. The friction coefficients they displayed ranged from 0.15 to 0.20 for dry conditions and from 0.05 to 0.11 for lubricated conditions [10]. As part of a broader study on solid polymeric lubricants, Ohta and Kanatsu published a small number of ball-cage friction measurements. A ball was fixed in a cage segment, and the cage was pushed with a load cell at a predetermined distance to measure the friction between the ball and the cage for three different cage designs. The findings of this study suggest that, for solid polymeric lubricants, cage design has a greater impact on bearing friction than load or speed. Furthermore, it was shown that bearing friction is increased by a greater contact area between the ball and cage pocket [11]. Approximate techniques have been employed by several other researchers to estimate cage friction. Measurements of the friction between balls and phenolic cage material were presented by Bertrand. He conducted his experiments using flat cage material pieces under various lubrication conditions and at varying speeds in contact with a revolving ball. At speeds of up to two meters per second, the friction coefficient values for three distinct lubricants and three different ball materials were shown. For lubricated contact between a ball and cotton-phenolic cage material, values varied from 0.06 to 0.15. Because of the beginning of starvation in the contact region, it was discovered that the coefficient of friction increased with speed from 0 to 1 m/s and remained constant at higher speeds. Every experiment involved applying 2N of load to the ball. According to Bertrand's research, ball material affects the friction coefficient to some extent in the boundary and mixed lubrication regimes, but its impact diminishes as full film lubrication is achieved. A different method was used by Brecher and two other researchers to estimate cage friction experimentally. For high-speed spindle bearings, bearing torque measurements were conducted using varying cage

designs and ball counts [12]. Then, by comparing the outcomes of the different studies, the cage's contribution to the total bearing torque was calculated. The researchers concluded that cage friction should not be disregarded when examining total bearing torque, despite the lack of stated coefficients of friction. They did this by highlighting the intricacy of the cage's contribution to overall bearing friction[12]. Analogous experiments were conducted as part of a study on cage friction and instability [13]. An experimental study on ball-cage clearance in bearings with polymeric cages was presented by Damien with his teammate. They mounted a modified nylon cage around the ball using a modified ball-on-disc technology. To investigate the impact of cage clearance on hunger and film thickness, the space between the ball and the cage was changed. They discovered that under oil lubrication, reducing the clearance between the ball and cage decreased the chance of hunger [14]. Grease showed the reverse effect: grease was better captured around the ball by a lower cage clearance [13]. Also, a new type of combined foundation consisting of diaphragm walls and pile groups was proposed recently, taking advantage of the benefits of both diaphragm walls and pile foundations. Finite element software is used to establish combined foundation models with diaphragm walls ranging from 1 m to 4 m in height and model tests are conducted to validate the reliability of the finite element results [15]

The literature study states that because this problem is crucial to the bearing design, it is necessary to investigate the stress distribution using finite element analysis [16]. The majority of the time, differing bearing types in different zones cannot be predicted by theoretical assumptions [17]. The current research paper investigated the tension analyses of different bearings under loading conditions.

2. Finite element analysis

To simulate the elliptical compression phenomenon, ANSYS R15 is implemented. The ISOTROPIC option is applied in ANSYS software for the material properties of bearings. The whole target is modeled as a three-dimensional medium. The inner and outer raceways are considered to be rigid and therefore the ANALYTICAL RIGID BODY characteristic is used for modeling of inner and outer raceways. Since the properties of the bearings are considered Chrome Steel - SAE 52100, the LINEAR ELASTIC option is applied in ANSYS to model the bearings as an elastic isotropic and homogeneous media. All edges of the target are pinned and the inner and outer raceways are allowed to translate only in vertical direction. The STEP option is used to model the loading and unloading processes during the contact phase. As the type of loading is statics, the STANDARD IMPLICIT option is selected. A surface-to-surface contact condition is defined for the raceways and the bearing in the INTERACTION option. It should be noted that the mentioned contact model follows the Hertzian contact law. The bearing is meshed by an eight-node continuum solid element (C3D8R). The target is composed of 4096 elements in its edge and its mesh size is condensed toward the contact area. The bias ratio is obtained as 5, according to a mesh sensitivity study to ensure that the results are converged reliably.

Two distinct simulation processes are used in this investigation. Two types of finite element simulations are available; I: is for the hertzian contact with subsurface stresses, and II: is for the subsurface stresses that include edge contacts. The results are obtained and provided in the results and discussions section following the modeling of the bearings and correspondingly various FEM conditions. The results and discussion section are divided into two subsections for reporting parts, I and II.

3. Results and discussions

To confirm the accuracy of the proposed finite element method, researchers will compare the first finite element results with theoretical predictions intended for the same contact geometry

[18]. Unlike theoretical models relevant to the same geometry, Figure 1 shows how the von Mises (Equivalent Stress) finite element findings do not display any edge loading. Furthermore, an elliptical Hertzian contact stress profile can be seen in a cross-section of the contact stress data (Figure 2). It is also evident from a closer look at the stress profile that the peak von Mises stress is not located close to the surface (Figure 3).

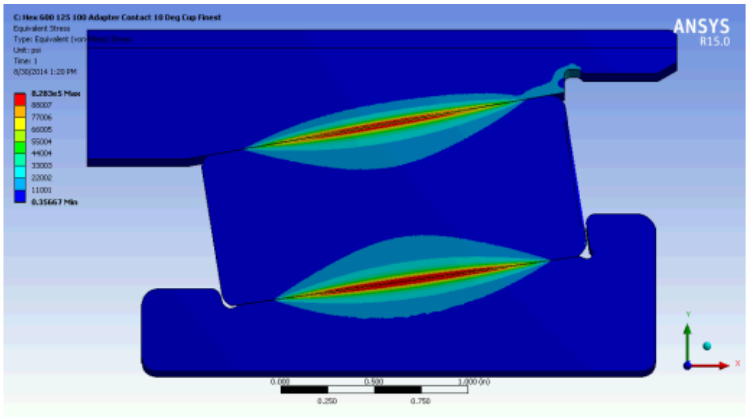

Figure 1: **von Mises Contact Stress Results for Primary Finite Element Model.**

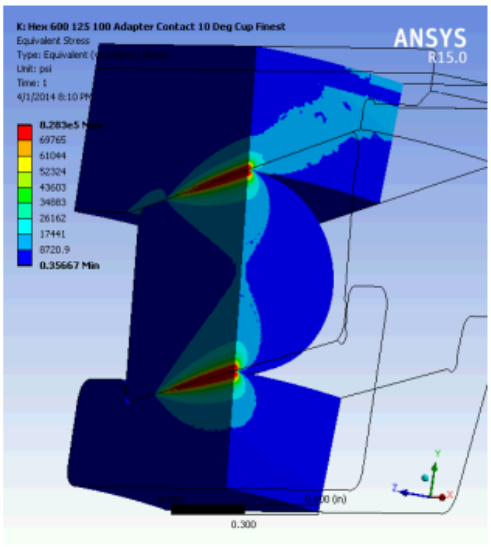

Figure 2: **Cross Section of von Mises Contact Stress Results for Primary Finite Element Model through Midpoint of Roller.**

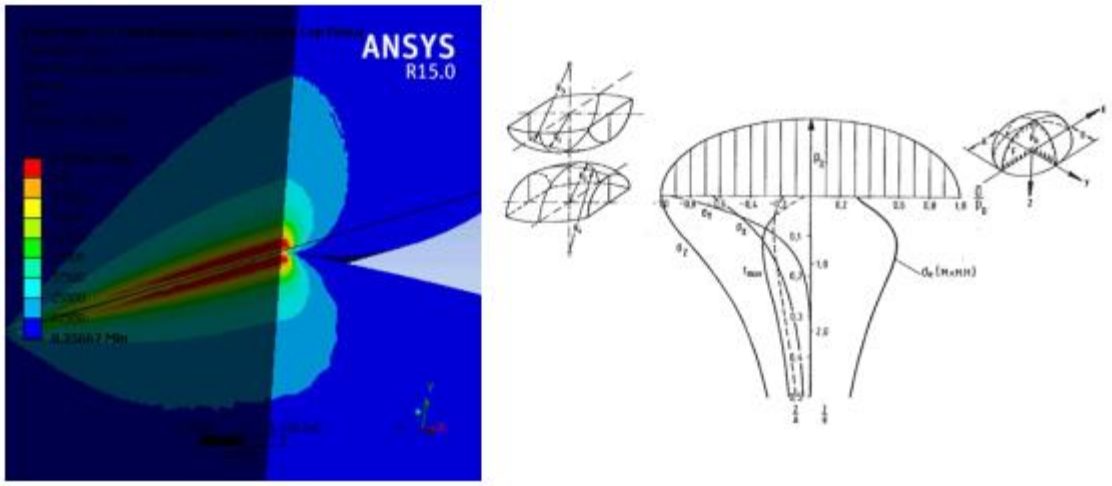

Figure 3: **Cross Section of von Mises Contact Stress Results for Primary Finite Element Model through Midpoint of Roller at Inner Raceway.**

The minimum principal stress results are also interesting if one accepts that the predominant mode of stress under bearing loads is compressive. Figure 4 shows that an elliptical contact stress profile is once more seen and that all of the bearing components are under compression as would be predicted.

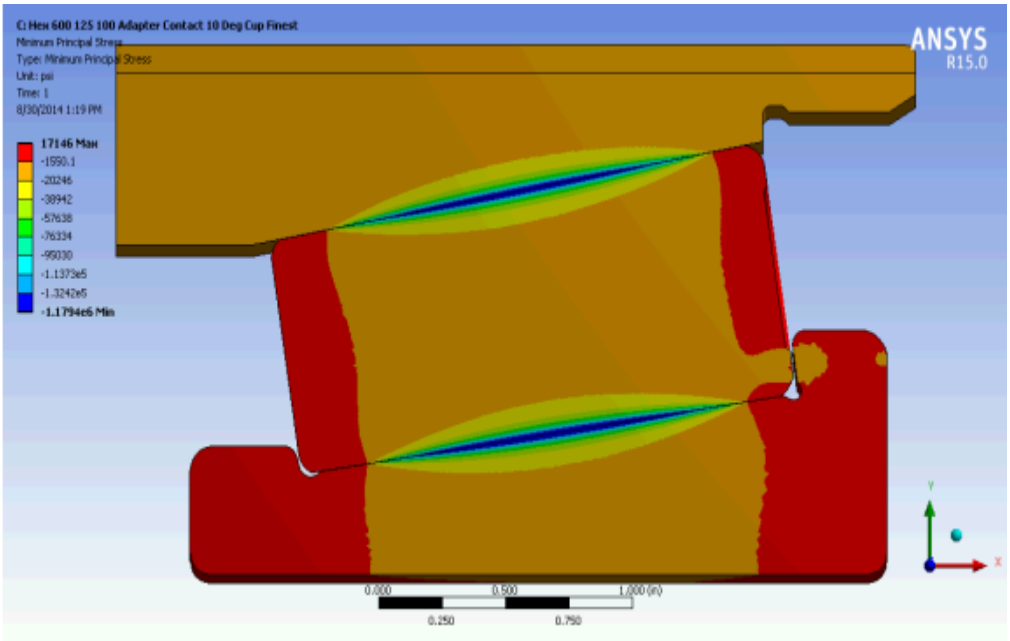

Figure 4: **Minimum Principle Contact Stress Results for Primary Finite Element Model.**

Lundberg and Palmgren estimate that preservation correlations continue to serve as the foundation for conventional industrial-bearing life projections, as was covered in the introduction. For the main simulation, the results of the maximum orthogonal shear stress, as reflected by Lundberg, are displayed in Figures 5 and 6. From these images, it is evident that the maximum orthogonal shear stress magnitude and depth may be found using finite element analysis. This kind of simulation technology might be utilized to improve bearing life prediction models for tapered roller bearings in the railroad sector with additional funding.

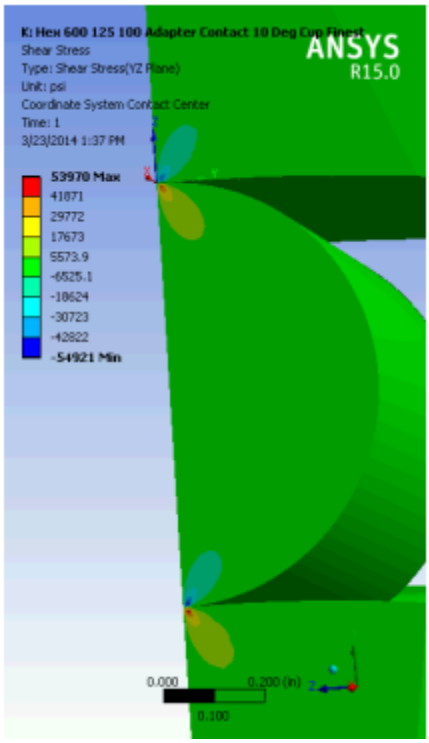

Figure 5: **Orthogonal Shear Stress Results in both Inner and Outer Raceway for Primary Finite Element Model.**

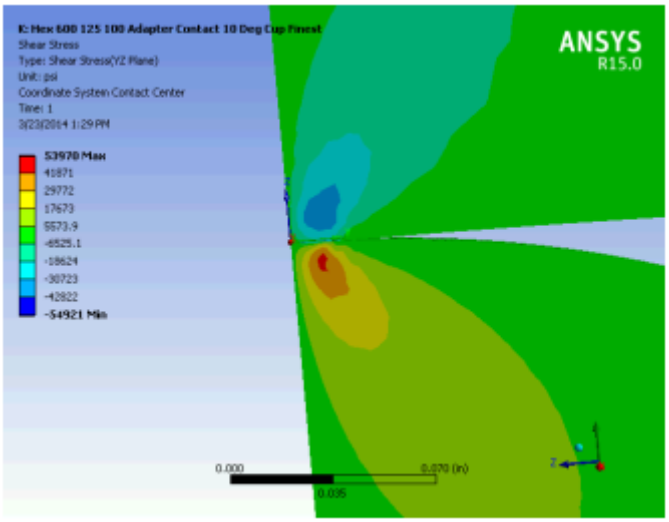

Figure 6: **Orthogonal Shear Stress Results in Outer Raceway for Primary Finite Element Model.**

The theoretical predictions were cross-checked with the numerical values of surface and subsurface stress at the center of every contact location[19], [20]. Below is the initial comparison of the contact pressure distributions at the component surfaces. Figure 7 shows the calculated Hertzian contact pressure along the semimajor axis of the contact ellipse between the roller and outer raceway. In the meantime, Figure 9 shows the Hertzian contact pressure projected along the semimajor axis of the contact ellipse between the roller and the inner raceway. For the inner and outer raceway maximum Hertzian contact pressure, there is a 4.2% and 9.4% discrepancy, respectively, between the theoretical predictions and the finite element data. It is believed that the outer raceway's deflection is the cause of the larger discrepancy between the pressure distribution between the roller and the outer raceway as determined by finite element calculations. As such, the crown's geometric alignment is not likely to be the cause. The deflection of the cup in Figure 8 indicates that, under the adapter load, the

component tends to gently deflect around the roller, suggesting that the flexible behavior of the cup may affect the contact stress profile. Not much flexure is needed to affect the contact geometry and consequent pressure distributions on precision ground-bearing components, despite the small deflection of the cup shown in Figure 8. The Hertzian theory does not take into consideration the bending of the elliptical surfaces in contact and instead assumes that the force between two elliptical bodies is entirely perpendicular to the contact plane.

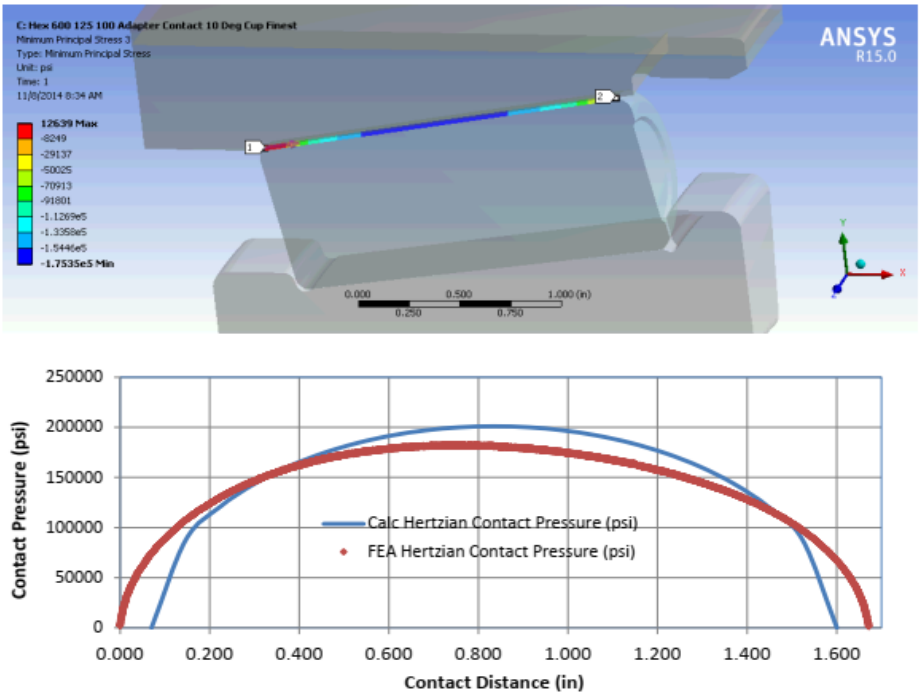

Figure 7: **Hertzian Contact Pressure between Outer Raceway and Roller along the Semimajor Axis of the Hertzian Contact Ellipse during Primary Finite Element Analysis.**

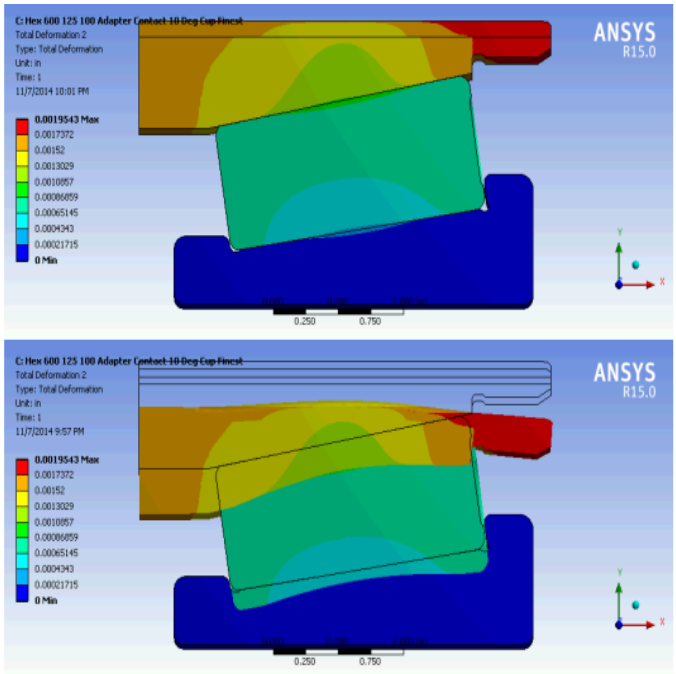

Figure 8: **Deflection of Outer Raceway during Primary Finite Element Analysis with Full Scale Results (top) and 200x Scaled Results (bottom) for Enhanced Demonstration.**

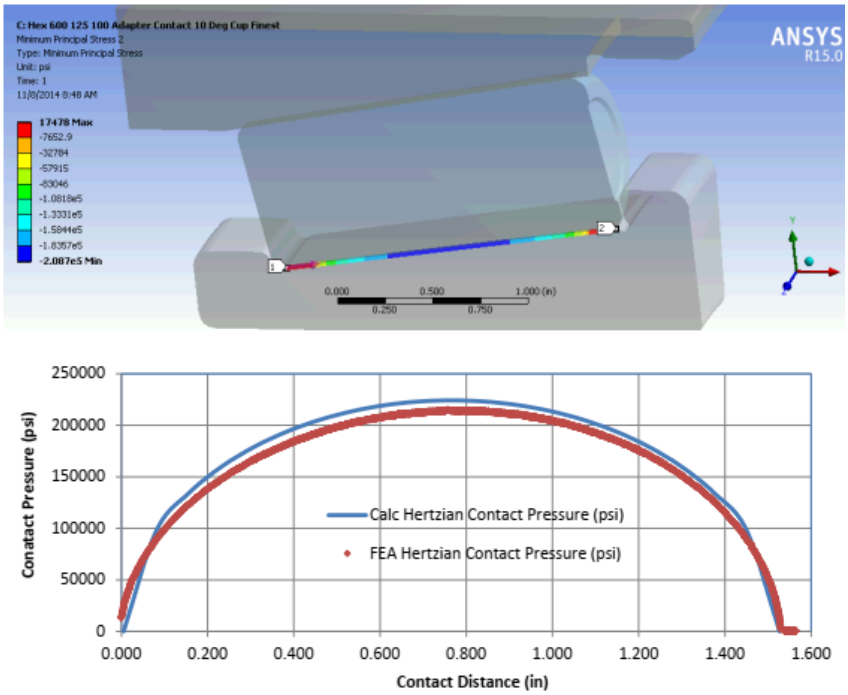

Figure 9: **Hertzian Contact Pressure between Inner Raceway and Roller along the Semimajor axis of the Hertzian Contact Ellipse during Primary Finite Element Analysis.**

Additionally, there is a fairly tight agreement between bearing theory and finite element when comparing Hertzian contact pressure values along the semi-minor axis of the contact ellipse (Figure 10 and Figure 11). However, the contact stress distribution along the semi-minor axis shows that the findings of the finite element method do not match with the theories. This could also be the cause of the little discrepancy in pressure maxima outcomes between finite element calculations and accepted bearing theory. This semi-minor axis length difference is thought to result from the model's components deflecting more compliantly than predicted by Hertzian theory, which assumes infinite radii and normal loads without bending, in order to mate with each other in contact.

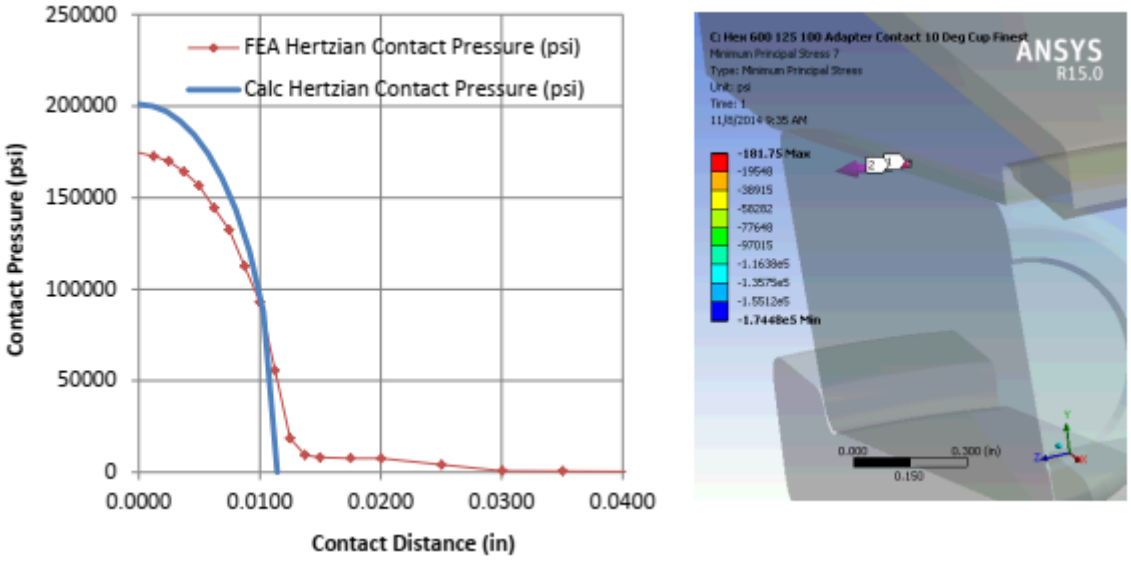

Figure 10: **Hertzian Contact Pressure between Outer Raceway and Roller along the Semi minor axis of the Hertzian Contact Ellipse during Primary Finite Element Analysis.**

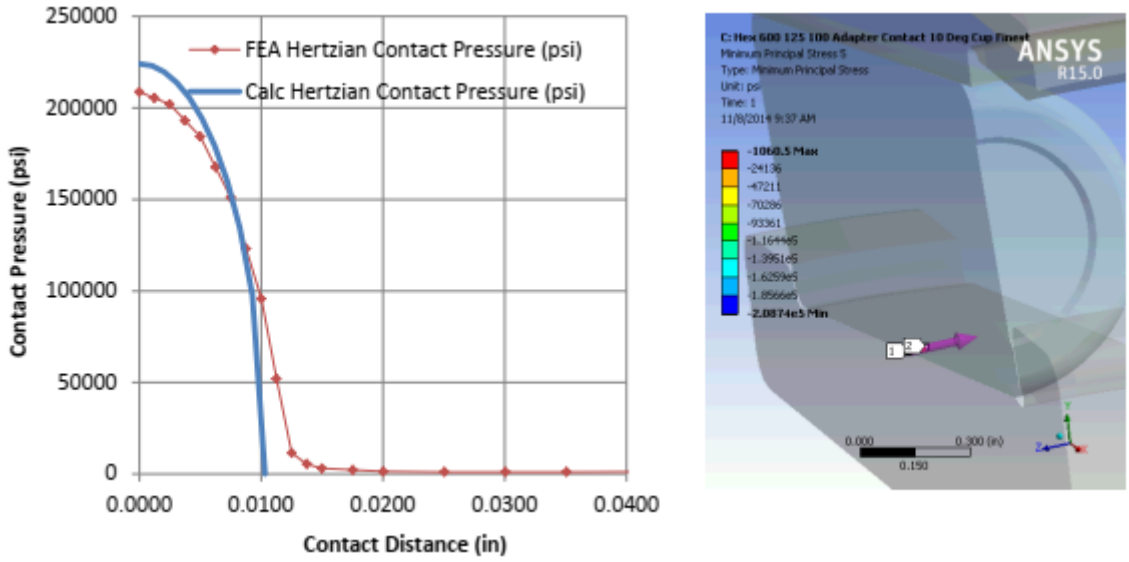

Figure 11: **Hertzian Contact Pressure between Inner Raceway and Roller along the Semi minor axis of the Hertzian Contact Ellipse during Primary Finite Element Analysis.**

Figures 12 and 13 show subsurface stress distributions along the roller crown's centerline. The finite element results for subsurface stress also closely match theoretical expectations. For the inner raceway contact, all magnitude and depth values matched within 10,000 psi and 0.001 inches, respectively, while the outer raceway contact showed a lower agreement between theory and finite element results. Subsurface stress measurements also show a larger divergence in peak surface pressure magnitude on the outer raceway compared to the inner raceway. Table 1 provides further information about the correlations between von Mises and maximum shear stress results. While the theory and primary finite element findings agreed quite well, other modeling methods were explored for reduced computing cost and increased accuracy; these are covered in the next subchapter.

Table 1: **Correlation between Primary Finite Element Method and Theoretical Predictions, Peak Maximum Shear Stress and von Mises Stress, Magnitudes and Depths.**

Subsurface Stress Results for Inner Raceway Contact			
Ultimate Stress Parameter	**Finite Element**	**Bearing Theory**	**% Difference**
Maximum Shear Stress Peak Magnitude (psi)	62915	67905	7.35%
Maximum Shear Stress Depth (in)	0.008	0.008	0.00%
von Mises Stress Peak Magnitude (psi)	116460	126152	7.68%
von Mises Stress Depth (in)	0.008	0.007	12.50%
Subsurface Stress Results for Outer Raceway Contact			
Ultimate Stress Parameter	**Finite Element**	**Bearing Theory**	**% Difference**
Maximum Shear Stress Peak Magnitude (psi)	52697	61651	14.52%
Maximum Shear Stress Depth (in)	0.008	0.009	11.11%
von Mises Stress Peak Magnitude (psi)	98871	114504	13.65%
von Mises Stress Depth (in)	0.008	0.008	0.00%

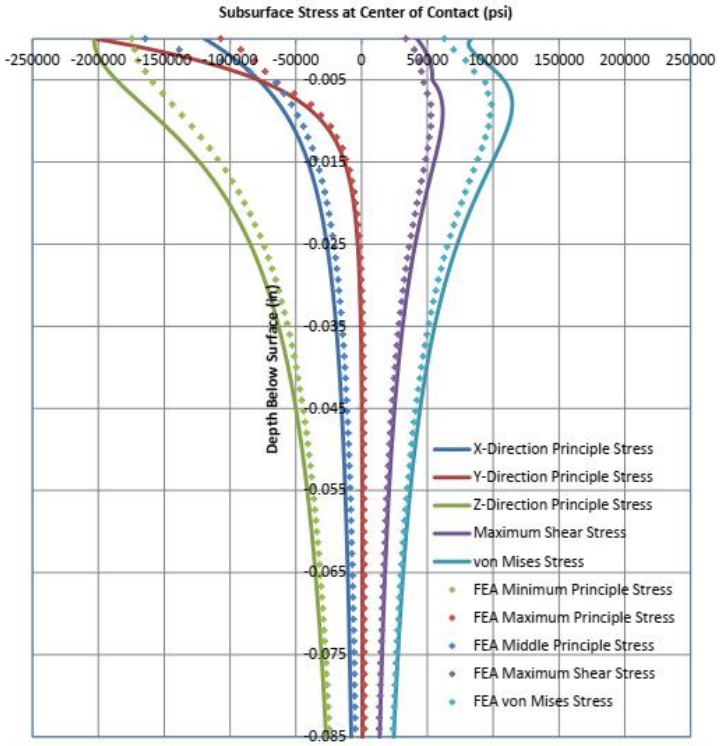

Figure 12: **Subsurface Stress between Outer Raceway and Roller at Center of the Contact during Primary Finite Element Analysis.**

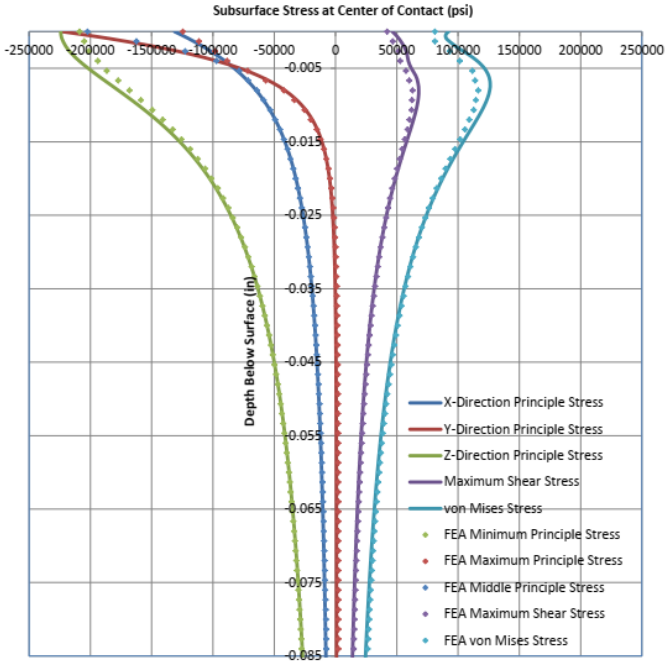

Figure 13: **Subsurface Stress between Inner Raceway and Roller at the Center of the Contact during Primary Finite Element Analysis.**

Increasing the contact relevance between the roller and the back rib of the cone to 75%, decreasing the size and refinement of the partitioned surfaces near the raceway contacts to a refinement level of two, decreasing edge sizing in the raceway contacts to 0.00175 inches, reducing the refinement of the central axis of the roller crown to one, and adding subsurface refinements near the edges of the raceway for post-processing of subsurface stresses.

When the roller was allowed to position itself in the finite element model without the adjust-to-touch setting on the roller interface treatment with the back rib of the cone, a Hertzian point contact stress was created between the back rib of the cone and the large end of the roller, as displayed in Figure 14. The reaction force Q_f in this location is of interest and is shown in Figure 15. After studying the components of the force in Figure 15, it was discovered that the angle of the reaction force θ_f was in between that of θ_i and the average of the inner and outer raceway angles. However, it was much closer to θ_i than the average. Given that θ_f is nearly equivalent to θ_i, the reaction force seen by the roller from the inner raceway will not exactly equal that of the outer raceway. This is supported by the finite element results from the second finite element analysis presented in Table 2 as a percentage of the applied Stribeck load Q_{max}.

Table 2: **Forces inside the Bearing as a Percentage of the Applied Stribeck Roller Load.**

Force between Bearing Components	% of Stribeck Roller Load
Force between Outer Raceway and Roller Outer Diameter	101.57%
Force between Inner Raceway and Roller Outer Diameter	101.53%
Force between Roller End Face and Back Rib of Cone	3.37%

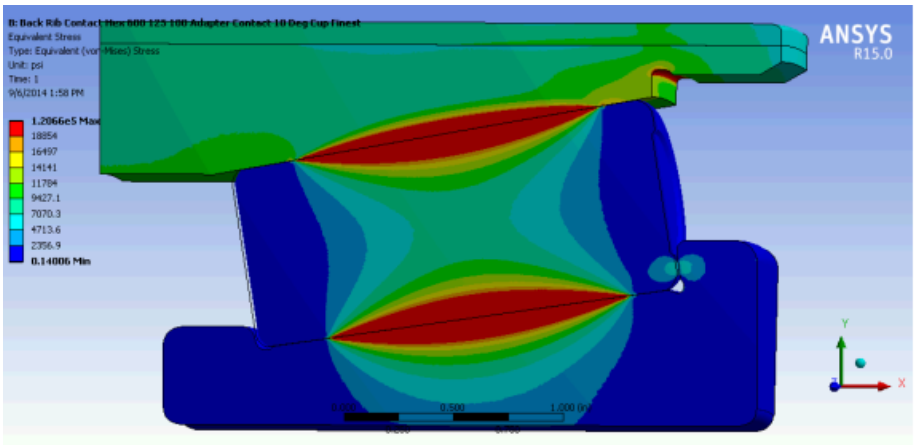

Figure 14: **Equivalent Stress Profile on Roller Including Cone Back Rib Contact in Second Finite Element Model.**

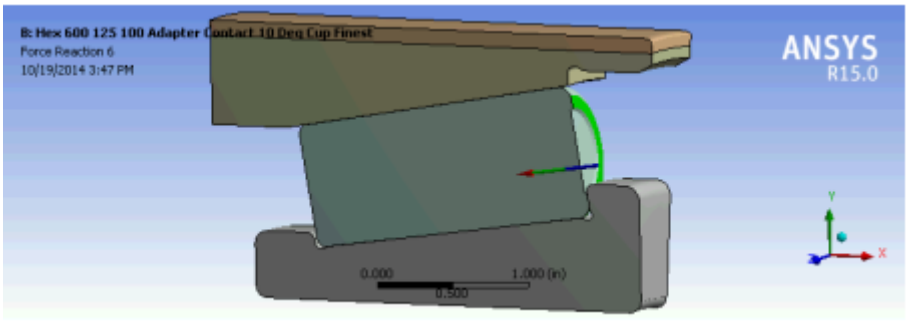

Figure 15: **Reaction Force Q_f on the Back Rib of the Cone from the Second Finite Element Model.**

The minimal principal stress results at the surface may be impacted to some extent by misalignment between the central axes of the outer raceway crown and the roller crown. But when comparing the obtained results, the misalignment of the crown geometry seems insignificant in comparison to the effect of the outer raceway displacement. Figure 17 shows an even greater agreement between theoretical and finite element findings. In the meantime, the second simulation improved the alignment between the roller and the cone crown in comparison to the first simulation.

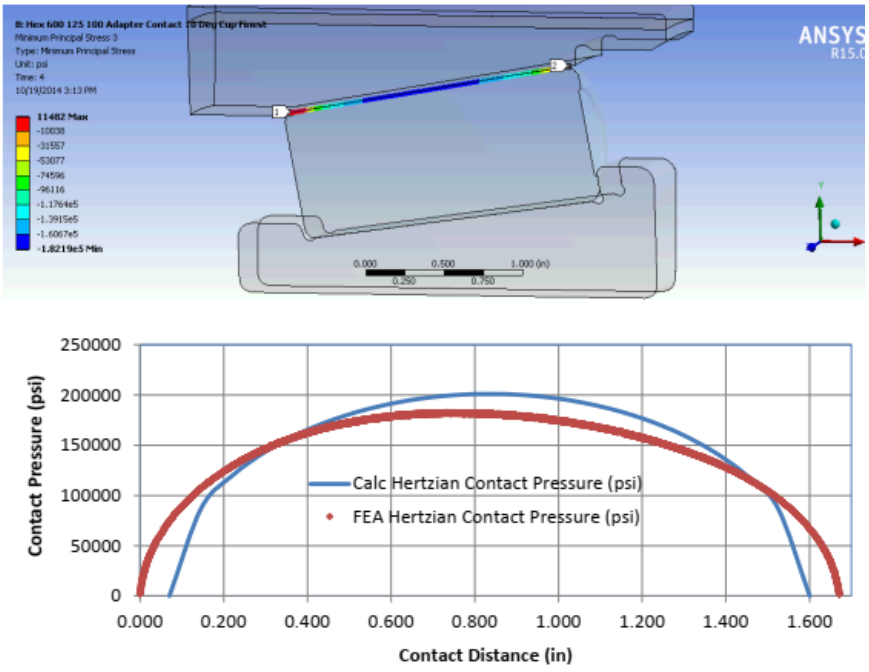

Figure 16: **Hertzian Contact Pressure between Outer Raceway and Roller along the Semimajor axis of the Hertzian Contact Ellipse for Second Analysis with Back Rib Contact.**

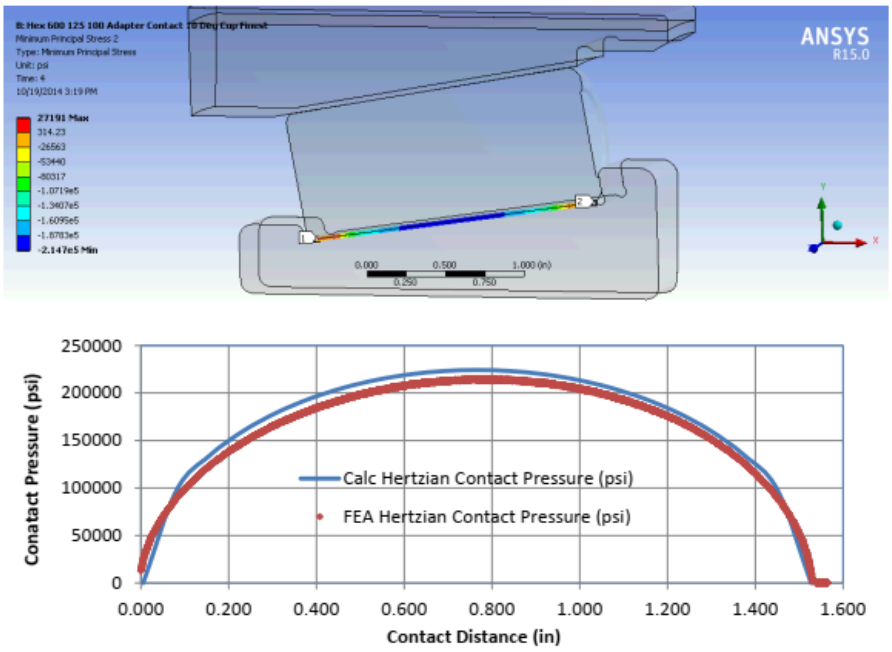

Figure 17: **Hertzian Contact Pressure between Inner Raceway and Roller along the Semimajor axis of the Hertzian Contact Ellipse for Second Analysis with Back Rib Contact.**

The subsurface stresses caused by roller contact with the inner raceway are depicted in Figure 18 with better crown geometry alignment. This indicates that, in the analysis of raceway subsurface stresses under frictionless contact, the impact of the back rib of the cone contact with the roller end appears to be negligible. Additionally, Table 3 compares the subsurface stress findings from the revised inner raceway alignment with the primary finite element results. It is evident that a stronger association between Hertzian theory and finite element methods is obtained with the second finite element approach.

On the other hand, as was indicated in the introduction, roller skewing may worsen the bearing's stress condition. The influence of the back rib contact on the roller in relation to roller skewing

is still a significant factor to take into account when making bearing design modifications, mostly because of frictional contact as observed in real bearing applications.

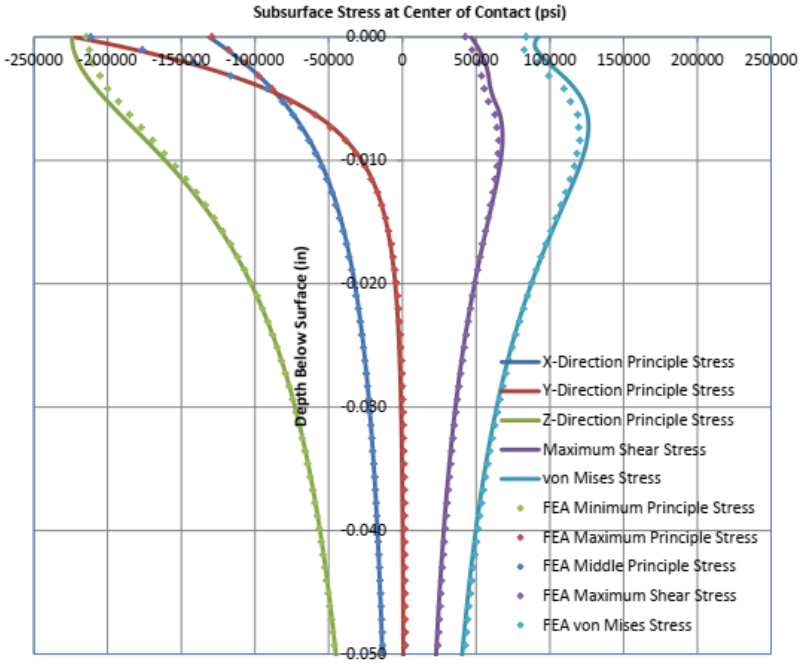

Figure 18: **Subsurface Stress between Inner Raceway and Roller at the Center of the Contact during the Second Finite Element Analysis with Back Rib Contact Included.**

Table 3: **Correlation between Finite Element Predictions of Peak Maximum Shear Stress and von Mises Stress, Magnitudes and Depths, for Primary and Second Finite Element Methods.**

Subsurface Stress Results for Inner Raceway Contact using Primary Finite Element Method			
Ultimate Stress Parameter	**Finite Element**	**Bearing Theory**	**% Difference**
Maximum Shear Stress Peak Magnitude (psi)	62,915	67,905	7.35%
Maximum Shear Stress Depth (in)	0.008	0.008	0.00%
von Mises Stress Peak Magnitude (psi)	116,460	126,152	7.68%
von Mises Stress Depth (in)	0.008	0.007	12.50%
Subsurface Stress Results for Inner Raceway Contact using Second Finite Element Method			
Ultimate Stress Parameter	**Finite Element**	**Bearing Theory**	**% Difference**
Maximum Shear Stress Peak Magnitude (psi)	65477	67,905	3.58%
Maximum Shear Stress Depth (in)	0.008	0.008	0.00%
von Mises Stress Peak Magnitude (psi)	120450	12,615	4.52%
von Mises Stress Depth (in)	0.008	0.007	12.50%

4. Conclusions

Surface stress values can also be affected by geometric changes in addition to differences in load circumstances. Two distinct bearing geometries were modeled under the same load as an additional example of how the unique finite element modeling methodology can be applied. As you can see in Figure 19, edge loading occurs in the low crown geometry load distribution along the semimajor axis of the Hertzian contact ellipse, but not in the high crown geometry. Additionally, as might be expected, the low crown geometry has a stronger roller taper influence on surface stress findings. To eliminate hostile edge loading scenarios and maximize raceway length usage, an optimal design for this load case may fall somewhere between the low crown and high crown profiles, assuming application loads stay constant. Edge loading can be predicted using classical Hertzian contact theory by comparing it to the raceway's length in the relevant design. However, finite element or other numerical approaches are required to calculate the amount of surface stress and subsurface stress under these conditions.

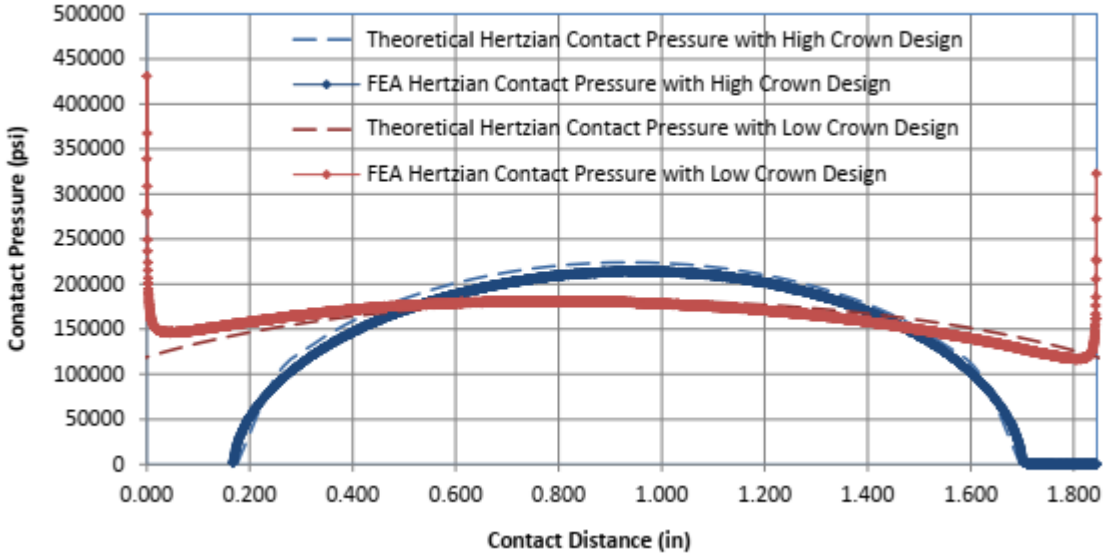

Figure 19: **Hertzian Contact Pressure between Inner Raceway and Roller along the Semimajor axis of the Hertzian Contact Ellipse for Two Different Tapered Roller Bearing Geometries Exposed to the same Stribeck Load (Distance along the Roller Surface Starting from the Small End (SE) on the Left at 0.000 inches).**

Disclosure Statement

No potential conflict of interest was reported by the author.

References

[1] Z. Liu, Y. Wang, L. Cai, Y. Zhao, Q. Cheng, and X. Dong, "A review of hydrostatic bearing system: Researches and applications," *Adv. Mech. Eng.*, vol. 9, no. 10, Oct. 2017, doi: 10.1177/1687814017730536/ASSET/IMAGES/LARGE/10.1177_1687814017730536-FIG20.JPEG.

[2] A. Gunduz, J. T. Dreyer, and R. Singh, "Effect of bearing preloads on the modal characteristics of a shaft-bearing assembly: Experiments on double row angular contact ball bearings," *Mech. Syst. Signal Process.*, vol. 31, pp. 176–195, Aug. 2012, doi: 10.1016/J.YMSSP.2012.03.013.

[3] C. Chaudhari, B. Thakare, S. Patil, and S. U. Gunjal, “A STUDY OF BEARING AND ITS TYPES,” 2015.

[4] G. G. Meyerhof, “Some Recent Research on the Bearing Capacity of Foundations,” *https://doi.org/10.1139/t63-003*, vol. 1, no. 1, pp. 16–26, Sep. 2011, doi: 10.1139/T63-003.

[5] R. K. Upadhyay, L. A. Kumaraswamidhas, and M. S. Azam, “Rolling element bearing failure analysis: A case study,” *Case Stud. Eng. Fail. Anal.*, vol. 1, no. 1, pp. 15–17, Jan. 2013, doi: 10.1016/J.CSEFA.2012.11.003.

[6] E. L. Salih, L. Gardner, and D. A. Nethercot, “Bearing failure in stainless steel bolted connections,” *Eng. Struct.*, vol. 33, no. 2, pp. 549–562, Feb. 2011, doi: 10.1016/J.ENGSTRUCT.2010.11.013.

[7] M. A. Molina and R. Gohar, “Hydrodynamic Lubrication of Ball-Bearing Cage Pockets,” *http://dx.doi.org/10.1243/JMES_JOUR_1978_020_004_02*, vol. 20, no. 1, pp. 11–20, Feb. 1978, doi: 10.1243/JMES_JOUR_1978_020_004_02.

[8] C. R. Gentle and M. Pasdari, “Measurement of Cage and Pocket Friction in a Ball Bearing for Use in a Simulation Program,” *ASLE Trans.*, vol. 28, no. 4, pp. 536–541, 1985, doi: 10.1080/05698198508981652.

[9] C. R. Gentle and R. J. Boness, “Prediction of Ball Motion in High-Speed Thrust-Loaded Ball Bearings,” *J. Lubr. Technol.*, vol. 98, no. 3, pp. 463–469, Jul. 1976, doi: 10.1115/1.3452889.

[10] S. Jiang, X. Chen, J. Gu, and X. Shen, “Friction moment analysis of space gyroscope bearing with ribbon cage under ultra-low oscillatory motion,” *Chinese J. Aeronaut.*, vol. 27, no. 5, pp. 1301–1311, Oct. 2014, doi: 10.1016/J.CJA.2014.08.005.

[11] H. Ohta and M. Kanatsu, “Running Torque of Ball Bearings with Polymer Lubricant (Effect of the Enclosure Form of Polymer Lubricant),” *Tribol. Trans.*, vol. 48, no. 4, pp. 484–491, Oct. 2005, doi: 10.1080/05698190500313478.

[12] C. Brecher, A. Hassis, and J. Rossaint, “Cage Friction in High-Speed Spindle Bearings,”

Tribol. Trans., vol. 57, no. 1, pp. 77–85, 2014, doi: 10.1080/10402004.2013.843738.

[13] H. Girish and R. Pai, "Theoretical investigation of the effect of offset loads on the static characteristics of a multi-pad adjustable bearing geometry," *Aust. J. Mech. Eng.*, vol. 20, no. 3, pp. 866–874, May 2022, doi: 10.1080/14484846.2020.1760435.

[14] B. Damiens, A. A. Lubrecht, and P. M. Cann, "Influence of Cage Clearance on Bearing Lubrication©," *Tribol. Trans.*, vol. 47, no. 1, pp. 2–6, 2004, doi: 10.1080/05698190490279128.

[15] D. Yousheng, Z. Keqin, L. Wenjie, Y. Zhigang, and Z. Huiling, "Bearing performance of diaphragm wall pile combination foundation under vertical and horizontal loads," *J. Eng. Res.*, Sep. 2023, doi: 10.1016/J.JER.2023.09.003.

[16] H. Molatefi, S. Najafian, and H. Mozafari, "Fracture mechanics of planetary gear set by using extended finite element method-linear elastic fracture mechanics approach," *Aust. J. Mech. Eng.*, vol. 13, no. 2, pp. 87–96, Jan. 2015, doi: 10.7158/M13-077.2015.13.2.

[17] A. Belhocine and A. Afzal, "Computational finite element analysis of brake disc rotors employing different materials," *Aust. J. Mech. Eng.*, vol. 20, no. 3, pp. 637–650, May 2022, doi: 10.1080/14484846.2020.1733175.

[18] S. H. Gawande, K. Balashowry, K. A. Raykar, and K. H. Munde, "Estimation of contact stresses in EN31 rolling contact bearings for screw compressor using Gauss quadrature & statistical analysis," *Aust. J. Mech. Eng.*, Apr. 2023, doi: 10.1080/14484846.2023.2195098.

[19] M. A. Gharaibeh, H. Tlilan, and B. M. Y. Gharaibeh, "Stress concentration factor analysis of countersunk holes using finite element analysis and response surface methodology," *Aust. J. Mech. Eng.*, vol. 19, no. 1, pp. 30–38, Jan. 2021, doi: 10.1080/14484846.2019.1565069.

[20] R. Gou, X. Zhang, W. Yang, and X. Chang, "Finite element analysis of surface indentation on turbo-drill thrust ball bearing," *Aust. J. Mech. Eng.*, vol. 18, no. 3, pp. 385–394, Sep. 2020, doi: 10.1080/14484846.2018.1531811.